Engineering with Computers (2015) 31:237–257
DOI 10.1007/s00366-013-0344-8

ORIGINAL ARTICLE

Trimming of 3D solid finite element meshes: sheet metal forming tests and applications

P. D. Barros · A. J. Baptista · J. L. Alves · M. C. Oliveira · D. M. Rodrigues · L. F. Menezes

Received: 13 June 2013 / Accepted: 14 October 2013 / Published online: 26 October 2013

Abstract Over the last years, the numerical simulation of integrated processes has become the major challenge in virtual try-out of sheet metal components, including trimming operations that may occur between forming steps. Detailed simulation of trimming processes is a challenging task, particularly when integrated with other forming operations such as deep drawing or hemming. A simplified approach can be adopted in which elements outside the trim surface are deleted from the finite element (FE) model adjusting the remaining to the surface. Following this approach, the state variables are mapped from the old FE mesh to the new trimmed mesh to continue the simulation. This paper addresses this simplified approach to the trimming process exploring a previously presented algorithm (Finite Elem Anal Des 42: 1053–1060, Baptista et al. 2006), which allows the treatment of hexahedral finite element meshes. Particularly, it focuses on the performance evaluation of the implemented strategies for correcting the FE mesh to the trimming surface, including the treatment of pentahedral-shaped elements. Different correction and treatment strategies are evaluated on different types of meshes, based on numerical simulation results of simple mechanical tests: uniaxial tensile test and simple bending test. Finally, two practical applications are given where the local effect of the trimming algorithm is highlighted.

Keywords Trimming · Solid finite elements · 3D hexahedral meshes · Multi-step forming

P. D. Barros (✉) · M. C. Oliveira · D. M. Rodrigues · L. F. Menezes
Department of Mechanical Engineering, CEMUC, University of Coimbra, Polo II, Rua Luís Reis Santos, Pinhal de Marrocos, 3030-788 Coimbra, Portugal
e-mail: pedro.barros@dem.uc.pt

A. J. Baptista
INEGI, Institute of Mechanical Engineering and Industrial Management, FEUP Campus, Rua Dr. Roberto Frias, 400, 4200-465 Porto, Portugal

J. L. Alves
Department of Mechanical Engineering, University of Minho, Campus de Azurém, 4800-058 Guimarães, Portugal

1 Introduction

Nowadays the finite element method (FEM) is one of the most popular tools used to solve all types of complex engineering problems. Among other mechanical engineering areas, the continuous development of FEM codes specifically dedicated to the numerical simulation of sheet metal forming processes has strongly contributed to reduce the long and costly trial-and-error tool design process. However, the present challenge is not only to simulate the forming processes but also the entire sequence of production stages, including the tasks between forming operations or even the optimization of the digital manufacturing process itself [2–4].

In the fabrication of an automotive panel several trimming operations can be performed between each forming stage. Therefore, to accurately simulate a multi-stage deep-drawing process, it is necessary to take into account these intermediate trimming operations. Typically, the blank trimming operations are performed resorting to shearing processes. The FEM simulation of these processes is still quite challenging and requires advanced constitutive damage laws and very refined FE models. Therefore, most of the FE studies concerning trimming/blanking processes focus on 2D models [5–7] and only a few exceptions on the analysis of 3D processes [8–10]. The development of

integrated numerical tools, able to simulate the complete sheet metal forming manufacturing processes is of paramount importance to answer the real needs of the automotive industry. In this context, a simplified approach can be adopted to estimate the global influence of the trimming stages in the sheet metal forming processes. In this approach the FE model for the cutting process considers only the trimming surface and adjusts the FE mesh to it. The state variables are mapped between the old and the new FE mesh and a new equilibrium configuration is determined. Thus, no local effects associated to the cutting process are taken into account.

The simplified approach is the one adopted in DD3TRIM (acronym of Deep-Drawing 3D TRIMming code) in-house code, which was specifically developed for trimming 3D solid finite element meshes and remapping the state variables [1]. The numerical simulation of multi-stage forming processes can be performed combining DD3TRIM with DD3IMP (acronym of deep-drawing 3D IMPlicit code) in-house code [11–14], used for FEM analysis of the forming stages. All the algorithms developed in DD3TRIM code allow the trimming of finite element meshes composed by eight-node solid finite elements. The solid elements can be trimmed using surfaces defined by planes, to execute simple straight cuts, or by NURBS surfaces, to attain more complex trimming geometries [1]. Although solid elements can strongly penalize the computational efficiency, when compared with shell elements, they show many advantages in sheet metal forming simulations. Among others, they allow an accurate evaluation of the contact forces, through a precise description of the contact evolution on both blank surfaces, as well as an accurate description of the thickness evolution. Also, they allow a good prediction of the through-thickness state variable gradients and can be important to guarantee the accuracy in springback simulation, when the ratio between the tool radius and blank thickness is lower than 5–6 [15].

Only a few references can be found in the literature that specifically addresses the subject of trimming finite element meshes and, in particular, for solid elements applied to describe blank sheets. The simplest way to trim a finite element mesh is to eliminate the undesired elements. This methodology was applied, for instance, in the work of Kawka et al. [3]. In case of methods where the trimmed FE mesh is precisely adjusted to the trimming line/surface, the studies of Coelho et al. [16] for shell element meshes and Dhondt [17] for solid hexahedral meshes can be referred. Dhondt developed a method based on adjusting and subdividing the trimmed elements, which can significantly increase the number of elements added to the final trimmed mesh, which has a negative impact on the calculation time. Also, elements with large variations in size can be created, as well as distorted elements, which are obviously undesirable in terms of numerical accuracy of the subsequent numerical simulations.

The methodology adopted in the present work to trim the solid finite element mesh consists, first, in removing all elements that are located in the region to be eliminated, and identifying the elements that are intersected by the trimming surface. In the second step, the spatial position of some nodes of the trimmed elements is adjusted, with a so-called stretching node technique. In this correction stage there is no element addition and the distortion level depends both on the strategy adopted to adjust the nodes position and the relative position between the trimmed element and the trimming surface. In some cases these elements can be more distorted and even acquire pentahedral shapes. To minimize the distortion of such pentahedral-shaped elements, a post-processing stage is adopted, using one of the following local treatment schemes: element subdivision, node distribution and element degeneration. Although the proposed algorithms were specifically developed for hexahedral 3D solid finite elements, they can also be applied to trim 2D shell element meshes, since this can be simply understood as a particular case of a solid finite element mesh, where the third dimension is removed from algorithms.

The application fields of this trimming algorithm are very diverse. It has been applied in the intermediate steps of standard multi-stage deep-drawing processes [18, 19], as well as a pre-processing technique for mesh generation purposes. As example, starting from a structured and regular initial mesh and removing and trimming the excessive volume, a FE mesh of an arbitrary geometry of an initial blank can be both straightforward and efficiently obtained [20, 21].

The main objective of this paper is to evaluate the impact, in the numerical simulation results accuracy, of the methodologies used to correct and treat the trimmed elements towards the trimming surface. Two simple mechanical tests were chosen to try to isolate the influence of the trimmed elements in the overall numerical simulation results: the uniaxial tensile test and the simple bending test. Two types of mesh specimens were used: extracted (trimmed) from a homogenous base mesh and regular meshes with different inner elements orientations. Both types were generated with three different orientations, α, to the longitudinal plane of the sample (15°, 30°, 45°). The trimmed specimens allow to obtain elements with different distortion levels along the trimmed edges and thus to measure the impact of the correction and treatment algorithms. The regular meshes with different inner elements orientations are used to evaluate the influence of the element orientation with respect to the load direction.

The remainder of the paper is divided into three major sections. In Sect. 2, a review of the trimming algorithm and the correction and treatment methodologies is presented.

Section 3 presents the numerical results obtained for the uniaxial tensile and simple bending tests, for the different mesh specimens. In Sect. 4, two trimming benchmarks are presented to highlight the local effect of the adopted trimming algorithm. Finally, in Sect. 5 the main conclusions are summarized.

2 The trimming algorithm

The adopted trimming algorithm is divided into three stages: pre-processing, correction and post-processing. In the first, all the required data for the trimming operation is collected and some preliminary tasks are conducted to organize and store the information about the mesh to be trimmed. The correction stage includes the element removal, based on the volume of the element belonging to the region of the mesh to be eliminated, and application of the chosen adjustment strategy to correct the trimmed elements. At the post-processing stage, a run check is carried out to identify and locally treat the pentahedral-shaped elements that were created during the correction stage. Finally, the new trimmed mesh file is produced. Table 1 presents DD3TRIM global algorithm, which is briefly described in the next three subsections. A detailed description of the algorithm can be found in Baptista et al. [1].

2.1 Pre-processing stage

In the pre-processing stage, all data required for the trimming operation is read from input files, namely: the mesh to be trimmed; the geometrical information about the trimming surface (plane or NURBS surface); the correction type to be applied to the trimmed elements; and the local treatment scheme for the pentahedral-shaped elements. Additional geometrical information about the eight-node solid finite element mesh is internally generated, mainly related to the construction of connectivity tables for the nodes, edges and facets of the elements.

After allocating all the necessary connectivity tables, the relative position of both nodes and elements to the trimming surface is determined and stored in two status tables. For each node, the $\text{STATUS}^{(\text{node})}$ table is generated with one of the following three statuses: “keep”, “eliminate” or “on surface”. The $\text{STATUS}^{(\text{element})}$ table is created with one of the following statuses assigned for each element: “to treat”, “keep” or “eliminate”.

The status of each node is determined using an algorithm based on the projection of the node on the trimming surface. The algorithm assumes that the trimming surface has been previously oriented towards the mesh side to be eliminated [1]. The status of each element is determined by counting the number of nodes that have the “eliminate” status. If the number of nodes with “eliminate” status is equal to eight, the element status is “eliminate”. Otherwise, if none of the nodes of the element has “eliminate” status, then the element status is “keep”. Finally, when the number of nodes to eliminate is greater than zero but lower than eight, the status “to treat” is assigned to the element.

2.2 Correction stage

At the beginning of the correction stage each element with status “to treat” is checked to decide if the element should be eliminated or kept in the final mesh. The decision is based upon the percentage of the volume of the finite element that has to be eliminated, $V^{\text{eliminate}}$. If this percentage is less or equal to 50 % the element is assigned with status “keep”. Otherwise, the element is assigned with status “eliminate”.

Three different correction strategies were implemented to adjust the nodes of the trimmed finite elements: one merely based on element elimination, labeled I, and two other that try to describe the trimming geometry accurately, labeled II and III. In correction type I all nodes and elements with status “eliminate” are suppressed from the mesh, creating an irregular mesh boundary. This correction type is used by some commercial and academic codes and is the base for the other two developed correction strategies (e.g. [17, 22]). Furthermore, this simple strategy can be useful in the practical manipulation of large models, allowing to perform rough eliminations of parts of the mesh before proceeding with smoothing trimming operations. In correction type II, nodes with “keep” status are orthogonally projected onto the trimming surface. Nevertheless, to assure that the domain of the mesh is kept in the thickness direction, additional corrections are undertaken to determine the new node positions. In correction type III, the new spatial position of nodes with “keep” status is obtained by determining the intersection of the finite element edge with the trimming surface, for a predetermined edge correction direction. This correction method is particularly recommended in situations where it is essential to maintain the orientation of the element edges, such as when trimming multi-material meshes, where it is indispensable to preserve the boundaries of each material [1]. A schematic illustration of the three correction types is presented in Fig. 1.

2.3 Post-processing stage

In the post-processing stage, the nodal coordinates and finite element connectivity tables of the mesh are updated, by suppressing all nodes and elements that have been assigned with status “eliminate”. Due to nodal adjustments performed in the correction stage, elements with pentahedral-shape can appear in the trimmed mesh (see Fig. 2a).

Table 1 DD3TRIM trimming algorithm

BEGIN

- Pre-Processing Stage -

- Read mesh, trimming surface and correction and optimization type options data
- Generate connectivity of Nodes, Edges and Facets
- Generate tables containing the status of nodes and elements:
  $\text{STATUS}^{(node)} = \{keep; eliminate; on\ surface\}$
  $\text{STATUS}^{(element)} = \{to\ treat; keep; eliminate\}$

- Correction Stage -

DO for all elements with status $\text{STATUS}^{(element)} = \{to\ treat\}$

- Calculate the volume of the element
  IF $V^{eliminate} > 50\%$ **THEN** $\text{STATUS}^{(element)} = \{eliminate\}$
  IF $V^{eliminate} \leq 50\%$ **THEN** $\text{STATUS}^{(element)} = \{keep\}$
- Select correction type
  IF Case I
  - Eliminate the nodes and elements with status $\{eliminate\}$

  IF Case II or Case III
  - Project the affected nodes towards the trimming surface. For Case II project nodes in the normal direction to the trimming surface and apply corrections towards the element facet. For Case III project nodes along element edge direction

    IF $\text{STATUS}^{(element)} = \{eliminate\}$ **THEN** move node with $\text{STATUS}^{(node)} = \{keep\}$

    IF $\text{STATUS}^{(element)} = \{keep\}$ **THEN** move node with $\text{STATUS}^{(node)} = \{eliminate\}$

END DO

- Post-Processing Stage -

- Update nodal coordinates and connectivity tables
- Select treatment scheme for elements with pentahedral shapes:

Treatment type labelled L	Subdivide the element into five smaller ones
Treatment type without label	Move the nodes of the exterior face of the element to the middle edge position
Treatment type labelled D	Degenerate the element

END

Therefore, to minimize the elements' distortion, a local treatment is performed only to the pentahedral-shaped elements. A more global and extensive treatment is not adopted to minimize the region affected by the correction operation and avoid affecting the inner mesh elements. This allows reducing the error that is always present in the remapping operation that transfers the state and nodal variables from the original to the trimmed mesh.

Three local treatment schemes are implemented. The first one, labeled L, consists in subdividing the element into five smaller ones, by inserting a regular element in the middle of the original pentahedral-shaped element (see Fig. 2b). This strategy tries to eliminate the wide 180° angle that exists at the exterior edge of the pentahedral-shaped element, but at the cost of creating some narrow angles in some edges of the new elements. The second option, not labeled, consists on moving the nodes of the trimmed face of the element to the middle edge position (see Fig. 2c). Finally, the third option, labeled D, consists in element degeneration, transforming the standard eight-node solid finite element into a six-node element, but with the connectivity of an eight-node element (see Fig. 2d).

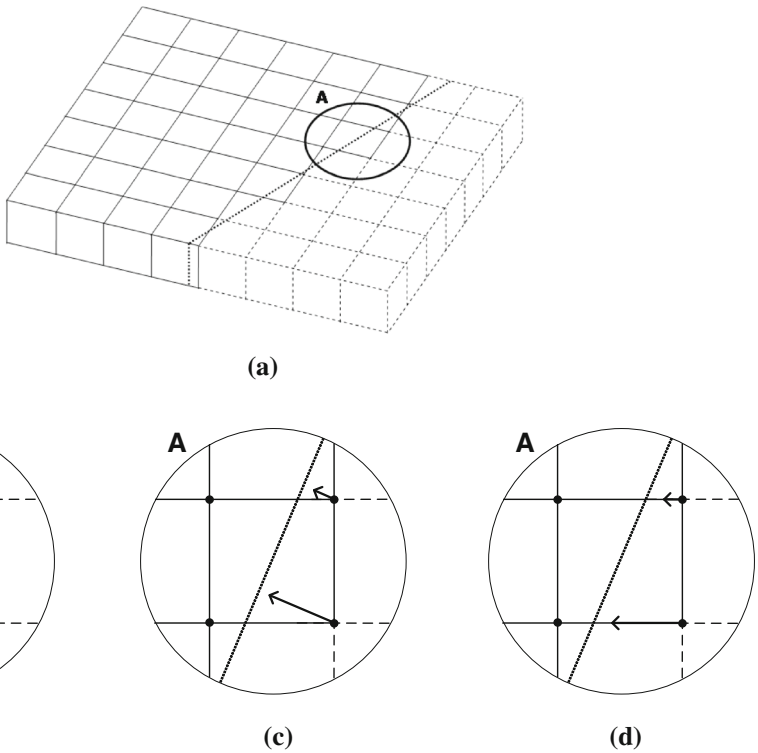

Fig. 1 Schematic representation of the trimming procedure and different correction types. **a** Trimming a regular mesh with a plane, represented by the *short dashed line*. The elements to be eliminated are represented by the *larger dashed line* and the elements to keep by the *solid line*. The nodes of the element identified in detail *A* are adjusted using correction: **b** type I; **c** type II and **d** type III

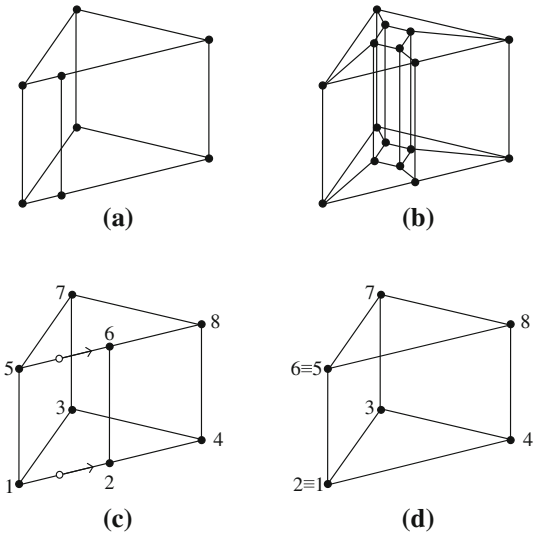

Fig. 2 Pentahedral-shaped elements treatment: **a** original element; **b** treatment type L (subdivided element); **c** element after node distribution (no label); **d** treatment type D (degenerated element)

3 Numerical simulation tests

The implemented correction and treatment methods can affect the shape of the trimmed elements and, subsequently, their performance in the numerical simulations. Therefore, to evaluate the suitability of the adopted solutions, some FE meshes were tested by simulating two simple mechanical tests: the uniaxial tensile test and the simple bending test. The simulations were performed using the DD3IMP (which stands for deep-drawing 3D IMPlicit code) static fully implicit in-house FE code, specifically developed to simulate sheet metal forming processes. The evolution of the deformation process is described by an updated Lagrangian scheme, based on the principle of virtual velocities proposed by McMeeking and Rice [23]. Contact with friction between the forming tools and the blank (deformable body) is based on a master–slave algorithm, with tools behaving as rigid bodies; friction is modeled by Coulomb's law. The contact with friction problem is treated by an augmented Lagrangian approach. For a given time increment $[t, t + \Delta t]$, an explicit algorithm is firstly used to calculate an approximate first solution for nodal displacements, state variables and frictional contact forces; a *r*-min strategy imposes several restrictions on the time increment size to improve both convergence rate and results accuracy [24]; finally, the explicit first solution is iteratively corrected, using a Newton–Raphson algorithm, to solve, in a single iterative loop, all problem non-linearities associated with both contact with friction problem and the constitutive behavior of the deformable body. The iterative procedure finishes when a satisfactory equilibrium in the deformable body is attained. It is then possible to update the blank sheet configuration, as well as all state variables, passing on to the calculation of the next time increment, until the end of the process [11–14].

3.1 Specimen description

The tested trimmed meshes were all obtained by cutting a regular mesh, with 2 mm in-plane element size, into small specimens measuring 100 × 20 × 1 mm. The mesh samples were trimmed with three different angles, α, with respect to the horizontal direction: 15°, 30°, 45° (see Fig. 3).

Correction method 'I' was not tested, since it cannot reproduce the geometrical borders of the specimens with accuracy. Correction methods 'II' and 'III' were combined with the different pentahedral-shaped element treatment methodologies to generate different trimmed meshes. The nomenclature used to describe the trimmed meshes is as follows: first, the correction method is identified followed by the treatment type. Thus, a mesh trimmed with correction method II and pentahedral-shaped elements treated by degenerating the element, is labeled 'II D'. If the pentahedral-shaped elements are treated by node distribution, no indication is added, leading to the label 'II'. Figure 4 presents the reference mesh as well as the trimmed meshes tested for correction method 'II' and 'III'. The meshes for pentahedral-shaped elements treated by element degeneration are not presented, since the finite element shape is the same for both treatment types. For α = 45°, only correction method 'II' was used due to obvious similarities between correction methods 'II' and 'III'. However, in this case an additional mesh was used in the tensile test example, which resorts to treatment type 'L' to correct the pentahedral-shaped elements (see Fig. 4g). The main objective of using this mesh was to evaluate the state variable gradients (and CPU time) obtained with this different shaped small elements (Fig. 4g), in comparison with the other meshes obtained by the other correction methods.

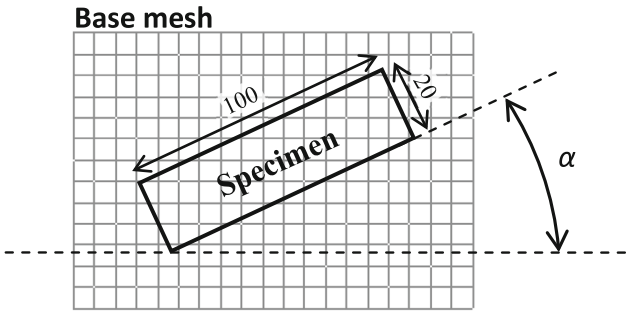

Fig. 3 Orientation of the trimmed mesh specimens

The inner finite elements of the trimmed meshes have an orientation with respect to the horizontal direction (tensile and bending loading direction) that is different from the reference mesh, as shown in Fig. 5a. To try to quantify separately the effect of the mesh orientation and of the trimmed elements, regular meshes with different inner elements orientations were also considered. Two different types of regular meshes were generated considering different orientations. In the first case, the finite element distribution along the horizontal direction is equal to the base mesh, presented in Fig. 5, and the distribution along the vertical direction is rotated by an angle α with respect to the base mesh vertical direction (see Fig. 5b). Thus, the label used for this type of mesh is always the rotation angle α followed by V. In the second case, the finite element distribution along the vertical direction is the same as the base mesh and the distribution along the horizontal direction is rotated by an angle α with respect to the one used in the horizontal direction of the reference mesh (see Fig. 5c).

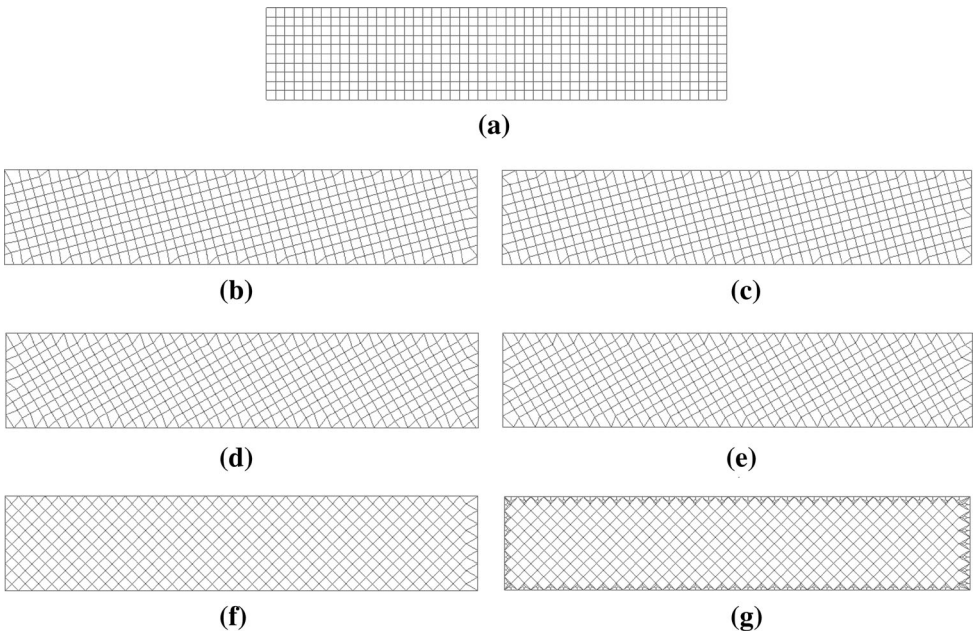

Fig. 4 2D representation of the trimmed meshes used in the elementary tests: **a** reference mesh with homogeneous element size (2 mm); **b** α = 15° (II); **c** α = 15° (III); **d** α = 30° (II); **e** α = 30° (III); **f** α = 45° (II); **g** α = 45° (L)

The label adopted for this type of mesh is always the rotation angle α followed by H. The distance between both directions was considered always equal to 2 mm, as also shown in Fig. 5. Thus, the parallelogram that defines the finite element in the plane presents equal length sizes a. The same three values were considered for the α angle in the generation of the V and H rotated meshes: 15°, 30°, 45°, and the tested meshes are presented in Fig. 6. These meshes use only degenerated elements in the border lines.

Considering the finite element aspect ratio as the in-plane longest to shortest side lengths, a, of an element, all meshes present a ratio equal to 1.0 for the inner elements. However, the rotated meshes length size changes with the rotation angle. To take this change into account, the in-plane finite element shape quality can be defined as

$$\mathrm{SQ} = 2A/\left(2a^2\right), \tag{1}$$

Where, A is the area of the parallelogram and a is the length size [25]. Table 2 presents the geometrical characteristics of the inner finite elements of the trimmed and rotated meshes. All trimmed meshes present the same SQ value of 1.0, which corresponds to the perfect reference finite element. For the rotated meshes the SQ value is always inferior to 1.0 and decreases with the increase of angle α. For these meshes the longest diagonal, d_2, is always longer than the one of the rotated meshes and increases with the increase of angle α. The shortest diagonal, d_1 is always shorter than the one of the rotated meshes and decreases with the increase of angle α. Thus, both diagonal values contribute to the decrease of the SQ value with the increase of angle α.

The mesh characteristics are presented in Table 3, where NE is the number of elements and NN the number of nodes. These characteristics are presented for meshes with one and two layers of elements in the thickness direction. The specimens with one layer are used in the tensile test example, while for the bending test it is necessary to consider at least two layers, to capture the through-

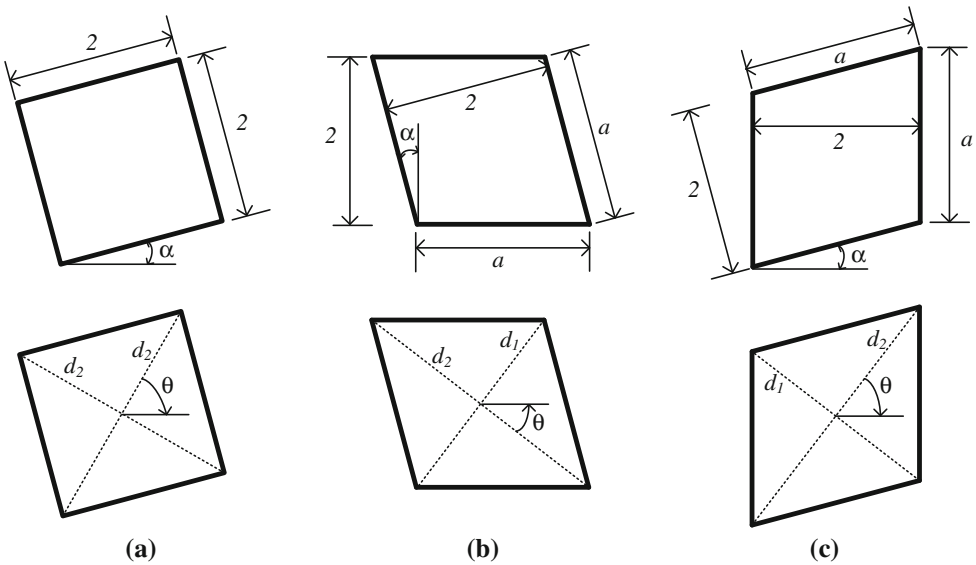

Fig. 5 Geometrical characteristics of the inner finite elements used in trimmed and rotated meshes: **a** trimmed mesh; **b** V mesh; **c** H mesh

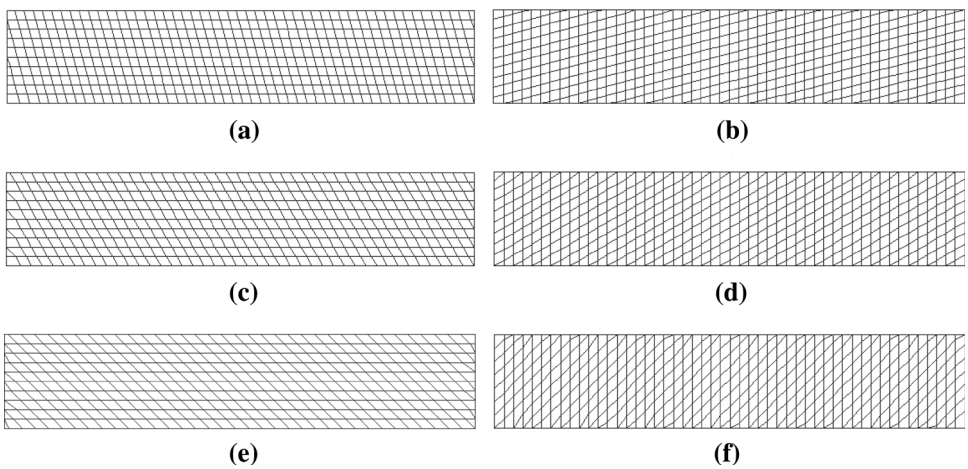

Fig. 6 2D representation of the rotated meshes used in the elementary tests. Mesh orientation: **a** $\alpha = 15°$ (V); **b** $\alpha = 15°$ (H); **c** $\alpha = 30°$ (V); **d** $\alpha = 30°$ (H); **e** $\alpha = 45°$ (V); **f** $\alpha = 45°$ (H)

Table 2 Geometrical characteristics of the inner finite elements used in trimmed and rotated meshes

Mesh type	Orientation α	a (mm)	d_1 (mm)	d_2 (mm)	A (mm^2)	SQ	θ
Trimmed mesh	0°	2.000	2.828	2.828	4.000	1.000	45°
	15°	2.000	2.828	2.828	4.000	1.000	60°
	30°	2.000	2.828	2.828	4.000	1.000	75°
	45°	2.000	2.828	2.828	4.000	1.000	90°
V mesh	15°	2.071	2.521	3.285	4.141	0.966	37.5°
	30°	2.309	2.309	4.000	4.619	0.866	30°
	45°	2.828	2.165	5.226	5.657	0.707	22.5°
H mesh	15°	2.071	2.521	3.285	4.141	0.966	52.5°
	30°	2.309	2.309	4.000	4.619	0.866	60°
	45°	2.828	2.165	5.226	5.657	0.707	67.5°

Table 3 Meshes characteristics

Mesh type	Layers	Orientation 15°		Orientation 30°		Orientation 45°	
		NE	NN	NE	NN	NE	NN
II	1	500	1,148	500	1,164	532	1,234
	2	1,000	1,722	1,000	1,746	1,064	1,851
II D	1	500	1,086	500	1,048	532	1,066
	2	1,000	1,629	1,000	1,572	1,064	1,599
III	1	501	1,152	500	1,164	–	–
	2	1,002	1,728	1,000	1,746	–	–
III D	1	501	1,088	500	1,048	–	–
	2	1,002	1,632	1,000	1,572	–	–
V	1	512	1,142	440	980	365	810
	2	1,024	1,713	880	1,470	730	1,215
H	1	546	1,190	475	1,020	406	858
	2	1,092	1,785	950	1,530	812	1,287
L	1	–	–	–	–	868	1,906
	2	–	–	–	–	1,736	2,859

NE number of elements, *NN* number of nodes

thickness stress gradients. The numerical prediction of bending results (i.e., force-displacement and springback angle) is quite sensitive to the in-plane mesh refinement and to the number of layers, being more accurate for a finite element mesh ratio (in-plane length divided by the through-thickness length) close to 1.0 [26, 27]. Taking into account the specimen thickness of 1.0 mm this requires an in-plane dimension (corresponding to the minimum distance between two nodes along the bending direction) of 0.5 mm. In fact, the reference mesh and all H meshes present a finite element mesh ratio equal to 4.0. The V meshes present a finite element mesh ratio always higher than 4.0, which increases with the increase of the θ angle. However, for the rotated meshes it is not easy to evaluate this parameter. Thus, the analysis is performed using the geometrical characteristics presented in Table 2. Although the results presented for the bending test are globally affected by the finite element mesh ratio, they allow the analyses of the influence of the implemented correction and treatment methods.

3.2 Material mechanical behavior

The constitutive equation that models the materials' mechanical behavior establishes the relationship between the most relevant state variables characterizing the continuum medium. The hypoelastic formulation of the generalized Hooke law is adopted,

$$\dot{\sigma}^{\mathrm{J}} = \mathbf{C}^{\mathrm{e}} : \mathbf{D}^{\mathrm{e}} \text{ or } \dot{\sigma}^{\mathrm{J}} = \mathbf{C}^{\mathrm{e}} : (\mathbf{D} - \mathbf{D}^{\mathrm{p}}), \tag{2}$$

where $\dot{\sigma}^{\mathrm{J}}$ is the rate of variation according to the Jaumann derivative of the Cauchy stress tensor $\boldsymbol{\sigma}$ and $\mathbf{D}$ the strain rate tensor, which can be decomposed into elastic and plastic parts, respectively $\mathbf{D}^{\mathrm{e}}$ and $\mathbf{D}^{\mathrm{p}}$. $\mathbf{C}^{\mathrm{e}}$ is the fourth-order elastic moduli which, for isotropic elasticity, is defined as

$$\mathbf{C}^{\mathrm{e}} = \frac{E}{1+\upsilon}\left\{\mathbf{I}_4 + \frac{\upsilon}{1-2\upsilon}\mathbf{I}\otimes\mathbf{I}\right\}, \tag{3}$$

where E is the Young modulus, υ is the Poisson coefficient, $\mathbf{I}_4$ and $\mathbf{I}$ are the fourth- and second-order identity tensors. The rate form of the elastoplastic constitutive equation is given by

$$\dot{\sigma}^{\mathrm{J}} = \mathbf{C}^{\mathrm{ep}} : \mathbf{D}. \tag{4}$$

$\mathbf{C}^{\mathrm{ep}}$ is the fourth-order elastoplastic moduli according to the constitutive model adopted (work-hardening laws and yield criterion). $\mathbf{D}$, the strain rate tensor, is the symmetric part of the velocity gradient $\mathbf{L}$.

Assuming that the constitutive model is formulated in the objective frame, all tensorial quantities are invariant. The global and objective frames are related throughout the rotation matrix $\mathbf{R}$, which is derived from the polar decomposition of the deformation gradient $\mathbf{F}$. The

evolution of the rotation tensor **R** during the process is governed by the differential equation

$$\dot{\mathbf{R}} = \mathbf{W}\mathbf{R} \text{ with } \mathbf{R}(0) = \mathbf{0}, \tag{5}$$

where **W** is the total spin tensor (anti-symmetric part of **L**) [28]. An associative plastic flow rule is adopted,

$$\mathbf{D}^{\mathrm{p}} = \dot{\lambda}\frac{\partial F(\bar{\sigma}, Y)}{\partial \boldsymbol{\Sigma}} \tag{6}$$

where $\mathbf{D}^{\mathrm{p}}$ is the plastic strain rate tensor, Y is the flow stress, $\bar{\sigma}$ is an equivalent tensile stress (computed from the chosen yield criterion) and $\boldsymbol{\Sigma} = \sigma' - \mathbf{X}$ is the effective deviatoric stress tensor. σ' is the Cauchy's deviatoric stress tensor and **X** is the back-stress tensor. $\dot{\lambda}$ is a plastic multiplier, which, when the yield function is a homogeneous function of degree one, can be demonstrated to be equal to the equivalent plastic strain rate, $\dot{\bar{\varepsilon}}^{\mathrm{p}}$, i.e., $\dot{\bar{\varepsilon}}^{p} = \dot{\lambda}$. The total equivalent plastic strain $\bar{\varepsilon}^{\mathrm{p}}$ is computed from the loading history as

$$\bar{\varepsilon}^{\mathrm{p}} = \int_0^t \dot{\bar{\varepsilon}}^{\mathrm{p}} dt = \int_0^t \frac{\boldsymbol{\Sigma} : \mathbf{D}^{\mathrm{p}}}{\bar{\sigma}} dt \tag{7}$$

The evolution law of **X** depends on the adopted kinematic hardening law. In this work kinematic hardening is not taken into account, i.e., $\boldsymbol{\Sigma} = \sigma'$. The yield function can be formulated in a generic form as

$$F(\bar{\sigma}, Y) = \bar{\sigma} - Y = 0 \tag{8}$$

$\bar{\sigma}$ is determined from the classical von Mises yield criterion, defined as

$$\bar{\sigma} = \sqrt{\frac{2}{3}\boldsymbol{\Sigma} : \boldsymbol{\Sigma}}. \tag{9}$$

The integration of the constitutive Eq. (4) at each material point allows to determine the increments of stress state ($\Delta\boldsymbol{\sigma}$) and equivalent plastic strain ($\Delta\bar{\varepsilon}^{\mathrm{p}}$). To determine these quantities, the consistency condition $\dot{F}(\bar{\sigma}, Y) = 0$ is imposed on the final configuration of time increment $[t, t + \Delta t]$. Due to constitutive behavior non-linearities, a Newton–Raphson algorithm is used. For further details readers are addressed to references [29, 30].

The numerical simulations were performed considering an elastoplastic material behavior, with isotropic work hardening described by the Swift law:

$$Y = K(\varepsilon_0 + \bar{\varepsilon}^{\mathrm{p}})^n \tag{10}$$

where K, ε_0 and n are material parameters. The material parameters considered are listed in Table 4.

Table 4 Material mechanical properties

Young modulus E (GPa)	221.37
Poisson coefficient υ	0.3
Yield stress Y_0 (MPa)	151.696
Swift law parameters	
K (MPa)	544.27
ε_0	0.0088
n	0.2703

3.3 Uniaxial tensile test

Figure 7 shows a schematic representation of the uniaxial tensile test. The test was performed considering an imposed

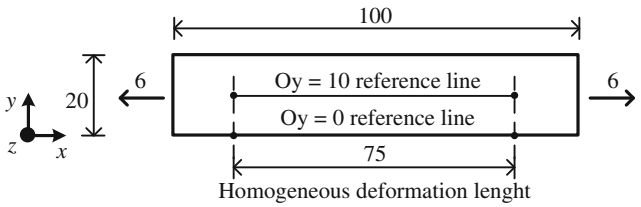

Fig. 7 2D schematic representation of the uniaxial tensile test

total displacement of 6 mm on each side of the specimen, in opposite directions (see Fig. 7). The nodes with imposed displacement are not allowed to move in any other direction. The force-displacement results obtained with the different meshes show almost negligible differences (see Fig. 8). However, the state variables' fields present some differences that are dictated by the correction/treatment type and the inner element orientation. The state variable selected to analyze the influence of these parameters was the equivalent plastic strain. Results are presented in the following subsections.

3.3.1 *Equivalent plastic strain distribution*

In this work a traditional tri-linear eight-node hexahedral finite element associated with a selective reduced integration scheme (SRI) is adopted [31–33]. Therefore, the integration of the constitutive equation is performed for eight integration points. In the following examples the equivalent plastic strain isocontours are plotted considering the values estimated for each node as follows

$$\bar{\varepsilon}^{\mathrm{p}}_{\mathrm{in}} = \frac{1}{\mathrm{Nel}}\sum_{i=1}^{\mathrm{Nel}} \bar{\varepsilon}^{\mathrm{p}}_{\mathrm{ig}^i}, \tag{11}$$

being Nel the total number of elements that share node in and ig^i the integration point linked (i.e., the closest) with a given node inside a given finite element. This transfer function corresponds to an arithmetic average, which is known to have a small smoothing effect in the equivalent plastic strain distribution. Anyhow, this smoothing effect is much smaller than if a reduced integration technique had been used (only one integration point per finite element).

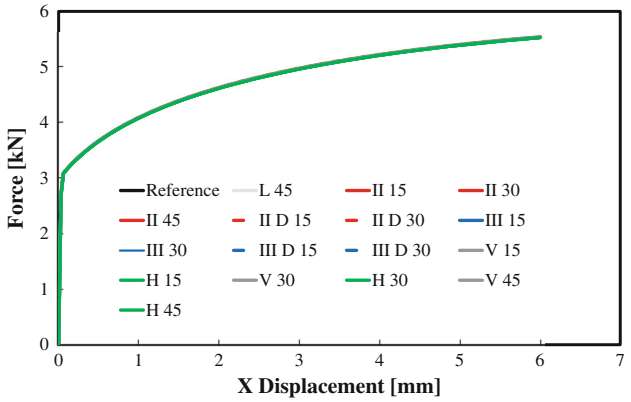

Fig. 8 Tensile force versus displacement in x direction for trimmed and rotated meshes

The equivalent plastic strain distribution, $\bar{\varepsilon}^{\mathrm{p}}$, at the end of the test is shown in Figs. 9, 10, 11, for meshes corresponding to orientations of 15°, 30° and 45°, respectively. To highlight the influence of the correction/treatment type a detail of the equivalent plastic strain distribution near the trimmed boundary is also presented, for each case.

From the analysis of the equivalent plastic strain distributions it is possible to observe that in the middle of the specimen there is no influence of the mesh orientation. However, even along the width symmetry line, close to the specimen border there are some differences in the plastic strain distribution. These differences are particularly visible when degenerated elements are used to replace the pentahedral-shaped elements or in case of 45° rotated meshes.

Along the horizontal border lines important differences are reported with respect to the reference mesh distribution. The trimmed elements with one node in the middle of the edge present always higher equivalent plastic strain values in those nodes, when compared with the reference mesh, for both correction types II and III. When degenerated elements are used, higher strain concentration values are also predicted, typically over a larger area. In some cases, an oscillation between higher and lower equivalent plastic strain values can also be observed, commonly associated to regions with strong transitions in element size. However, the presence of degenerated elements seems to intensify this effect. The 45° trimmed meshes present finite elements oriented in a symmetrical form towards the load direction. Thus, in this case it is possible to observe that the equivalent plastic strain distribution is similar to the one of the reference mesh whether degenerated elements are applied or not (Fig. 11b, c). The test conducted with decomposition of the pentahedral-shaped elements (treatment type L), presents irregular gradients in the border elements, highlighting the influence of the severe transition of geometry and dimensions between the border elements (see Fig. 11a). This type of solution requires a larger number of nodes, even when compared with the option of distributing the middle nodes of each pentahedral-shaped element (see Table 3). This has an impact on the CPU time, which is 2.32 times greater for the treatment type L mesh relatively to the II mesh.

3.3.2 Error analysis

To quantify the differences observed in the equivalent plastic strain distributions, the average equivalent plastic strain in the homogeneous deformation zone of the reference mesh (see Fig. 7) was calculated along two lines: (1) the inferior border line, labeled $Oy = 0$ and (2) the middle width of the specimen, labeled $Oy = 10$. The normalized percentage error between each mesh and the regular (reference) mesh was calculated along both lines as:

$$\mathrm{error}_{\varepsilon} = 100\left|\bar{\varepsilon}^{\mathrm{p}}_{\mathrm{ref}} - \bar{\varepsilon}^{\mathrm{p}}\right| \Big/ \left|\bar{\varepsilon}^{\mathrm{p}}_{\mathrm{ref}}\right|. \tag{12}$$

The maximum, average and minimum percentage error were calculated for each mesh on both lines and the results are summarized in Fig. 12.

Along the symmetry plane of the specimen ($Oy = 10$), the results show a percentage error always inferior to 3 %, for all meshes (see Fig. 12b, d, f). Since the error value is similar for both the rotated and the trimmed meshes, one can conclude that it is not related with the finite element ratio (SQ) but with the inner finite elements orientation. The percentage error increases for the border line ($Oy = 0$), in particular for the trimmed meshes (Fig. 12a, c, e). In fact, the meshes rotated along the vertical direction (V meshes) present a linear increase of the average percentage error with the increase of the α angle, with similar average values for both $Oy = 10$ and $Oy = 0$ lines. However, along the border line there is a slightly higher oscillation of the error values around the average. It is important to mention that these meshes have no degenerated elements along the horizontal border lines. The meshes rotated along the horizontal direction (case H) present a linear increase of the average error with the increase of the α angle between 15° and 30°, for both lines. However, for 45° the error along the $Oy = 10$ line stabilizes, while along the $Oy = 0$ line also increases. Also, in this case, it is possible to confirm higher deviations of the percentage error around the average value, particularly in the border line, which can be related with the different element sizes as well as with the presence of degenerated elements. The 45° trimmed mesh with treatment type L presents an error similar to mesh H although it has no degenerated elements. Thus, the comparison between 45° V mesh and L mesh highlights the importance of the finite element ratio in the border line. H meshes present irregular shaped elements in the border line, but also degenerated elements, which lead to a higher variation of the equivalent plastic strain values.

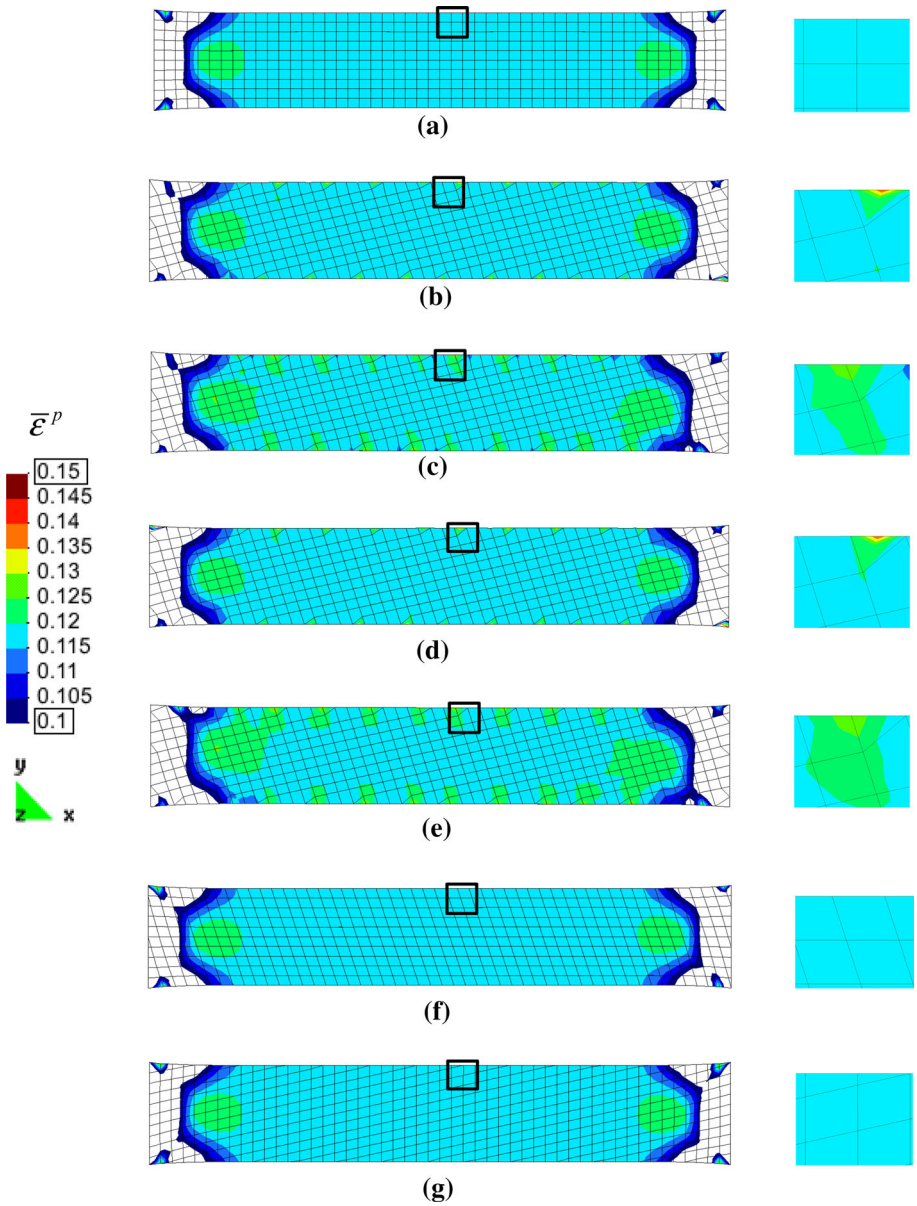

Fig. 9 Equivalent plastic strain distribution in the uniaxial tensile test for the reference mesh and meshes with orientation 15°: **a** reference mesh; **b** mesh II; **c** mesh II D; **d** mesh III; **e** mesh III D; **f** mesh V; **g** mesh H

The meshes trimmed with the node repositioning in the middle of the edge also present a linear increase of the percentage error with the α angle increase, along $Oy = 10$ line (see Fig. 12d). In this case, it is possible to confirm that the correction strategy III slightly increases the variation of the percentage error, but the difference is marginal. Along the border line the percentage error strongly increases for the 15° and 30° meshes, being higher for the 30° meshes. Along this line, the difference between both correction strategies is marginal (see Fig. 12c). The percentage error for the 45° trimmed mesh is similar between the $Oy = 0$ and the $Oy = 10$ lines since, globally, this mesh is more regular than the others.

When adopting degenerated elements along the border line, the percentage error slightly increases along the symmetry line. This increase is more evident for 15° and 45° trimmed meshes (see Fig. 12f). Along the border line the percentage error increases with the α angle for meshes with 15° and 30°. This can result from the fact that there are more degenerated elements in case of meshes with 30°. However, for the 45° mesh, the percentage error is similar to the one obtained with other 45° trimmed meshes, although all elements along the border line are degenerated. This can be related with the fact that for this particular case the node in the middle of the edge presents only a linear displacement (see Fig. 11). The comparison of the error obtained for trimmed meshes with and without degenerated elements allows confirming that the average error is similar. However, the use of degenerated elements reduces the error variations in the border line, while

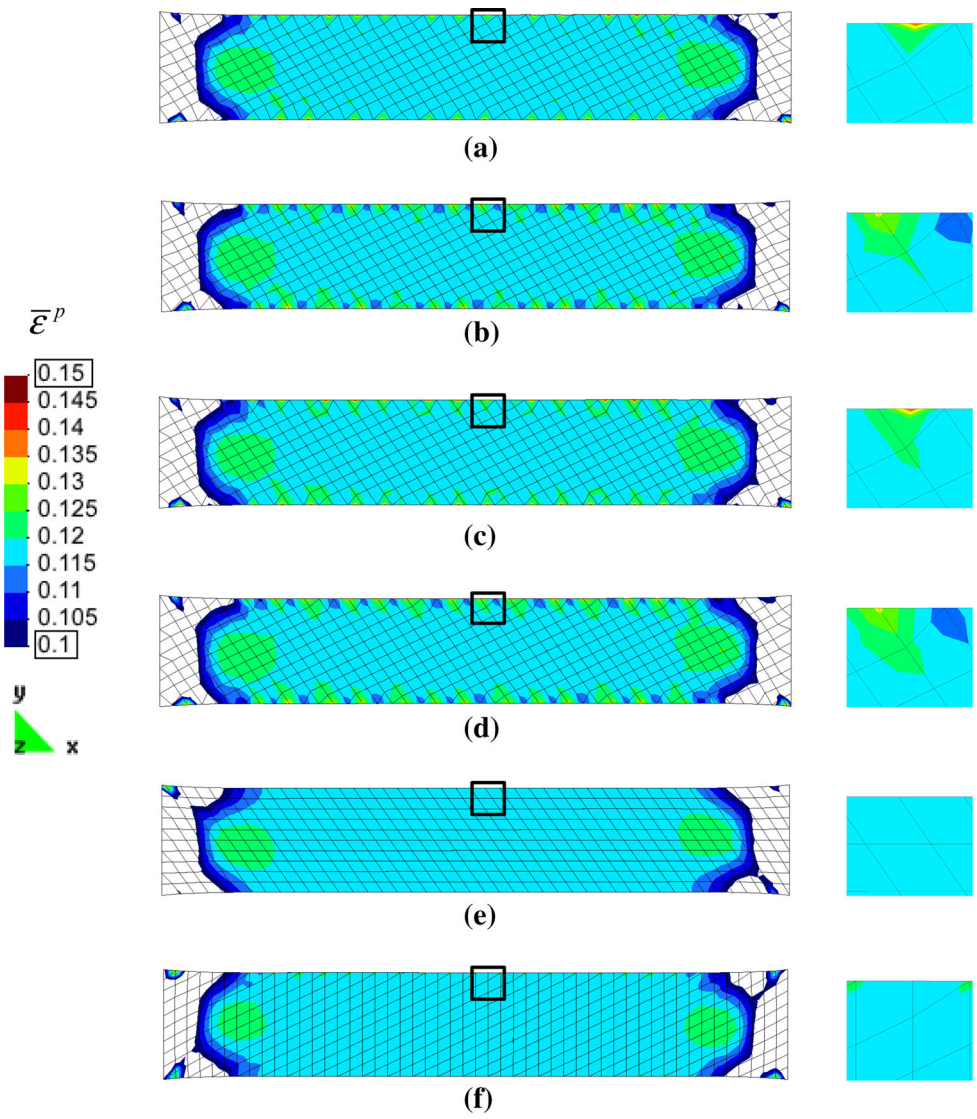

Fig. 10 Equivalent plastic strain distribution in the uniaxial tensile test for meshes with orientation 30°: **a** mesh II; **b** mesh II D; **c** mesh III; **d** mesh III D; **e** mesh V; **f** mesh H

slightly increases those variations along the symmetry line (see Fig. 12c–f).

Globally, the results allow to confirm that finite element misalignment to the tensile direction introduces an average percentage error inferior to 3 % along the symmetry line. The use of irregular shaped elements along the border line increases the percentage error variation (see, for instance, Fig. 12a). Higher error variations are obtained in the border line when degenerated elements are not adopted. However, the use of degenerated elements leads to a slightly higher error for the strain distribution in the inner elements.

3.4 Simple bending test

Figure 13 shows a schematic representation of the bending test. The test was performed by controlling the displacement, d, in one end of the specimen, until a nominal deflection of 50 mm. The nodes in the opposite end were constrained in all directions and plane strain conditions were imposed in the width direction.

For this test, the force-displacement results obtained with the different meshes present some important differences. Thus, in the following subsections the differences obtained in the force-displacement evolution, the equivalent plastic strain distribution and the springback angle β, as defined in Fig. 13, are discussed.

3.4.1 Force–displacement evolution

The force–displacement results obtained with the different trimmed and rotated meshes are shown in Fig. 14, together with the regular reference mesh result. Figure 14a presents the comparison between the reference mesh results and the trimmed meshes. Since no relevant differences are noticed between the different trimming cases and local element treatment schemes, the force evolution curves are only

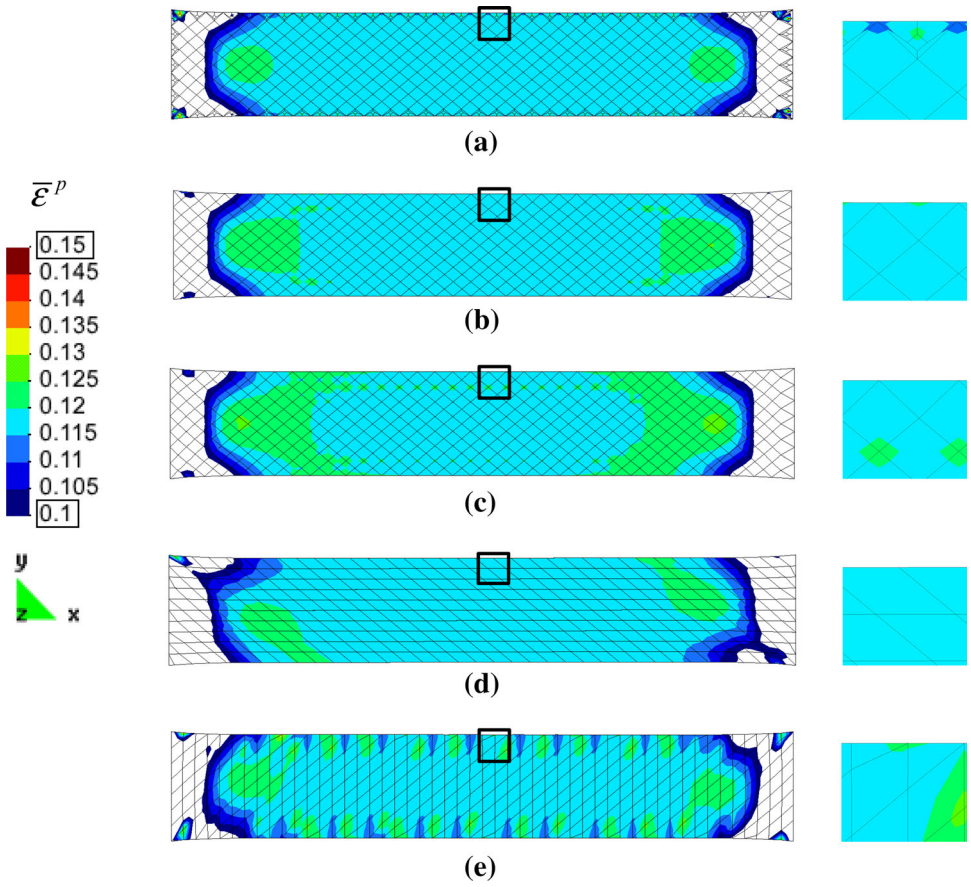

Fig. 11 Equivalent plastic strain distribution in the uniaxial tensile test for meshes with orientation 45°: **a** mesh L; **b** mesh II; **c** mesh II D; **d** mesh V; **e** mesh H

grouped according to the trimming orientation. Figure 14b presents the comparison of results between the reference mesh and the rotated meshes, using a different scale due to the results obtained with the V meshes. From the analysis of the figure it can be concluded that the inner finite element orientation of the mesh directly affects the numerical prediction of the force evolution. For the trimmed meshes, higher rotation angles induce smaller bending force values. For the rotated meshes, two different behaviors occur. In case of H meshes, the force evolution is marginally affected by the finite element orientation, while for V meshes higher rotation angles induce greater bending force values.

These results can be explained considering the orientation of the longer diagonal of the inner finite element of each mesh, θ, as represented in Fig. 5. The θ angle is defined as the minimum angle between the longer diagonal, d_2, of the finite element and the horizontal direction. The values for this angle are reported in Table 2, for each mesh. From the analysis of the table it is possible to confirm that this angle is smaller for the rotated V meshes, indicating that the longer element diagonal is more aligned with the bending direction. Since the longer diagonal value also increases with the rotation angle α, the values predicted for the force evolution also increase. For the rotated meshes the value of the diagonals is always the same. However, with the increase of the rotation angle α, the diagonals are less aligned with the bending direction, leading to the decrease of the bending force value. This conclusion can be arguable, since for the 45° rotation angle one of the diagonals is totally aligned with the horizontal direction. However, in this case, there is always an equidistant node to both nodes aligned with the bending direction, which seems to contribute to the decrease of the finite element mesh stiffness.

3.4.2 Equivalent plastic strain distribution

The equivalent plastic strain distribution was also analyzed for the different meshes and compared with the reference mesh results, using Eq. (11) to transfer the information from integration points to nodes. Figures 15, 16 and 17, present the results for the orientations of 15°, 30° and 45°, respectively. These figures show a detail of the part close to the fixed end, since the differences in the rest of the specimen are negligible. From the analysis of these figures it is observed that the strain distribution is clearly dependent on the FE orientation, since none of the other meshes can accurately reproduce the strain distribution observed for the reference mesh. Near the fixed boundary all the trimmed meshes and the H meshes show smaller strain

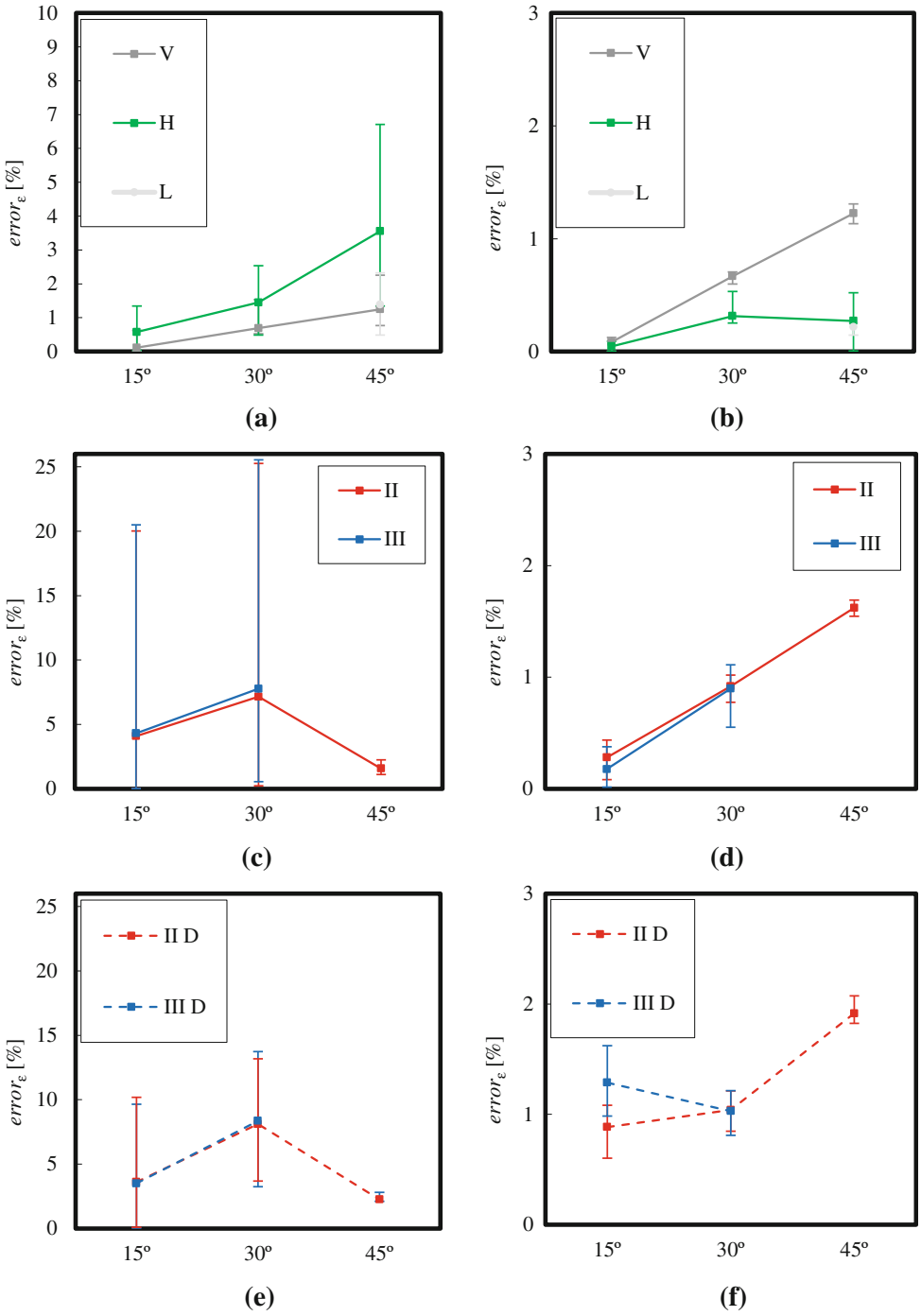

Fig. 12 Percentage normalized error determined for the uniaxial tensile test. Rotated meshes V and H and treatment type L: **a** $Oy = 0$; **b** $Oy = 10$. Trimmed meshes with correction type II and III and treated nodes located in the middle edge: **c** $Oy = 0$; **d** $Oy = 10$. Trimmed meshes with correction type II and III and treatment type D: **e** $Oy = 0$; **f** $Oy = 10$

values than the reference mesh. The V meshes present increasing equivalent plastic strain values with the rotation angle, near the fixed boundary, which can be explained taking into accounting the same effects seen in the previous subsection.

Comparing the results for the meshes created using the different correction types, subtle differences can be seen. For the 15° trimming orientation, the correction type II seems to induce lower oscillations in the equivalent plastic strain, for nodes in the middle of the facet of corrected elements (see Fig. 15c, e). The option of degenerating the pentahedral-shaped elements slightly improves the results for this correction type (Fig. 15f). For the 30° trimming orientation, the correction type III (Fig. 16a, c) appears to be the more adequate and the use of degenerated elements also seems to lead to an equivalent plastic strain distribution closer to the one obtained for the reference mesh.

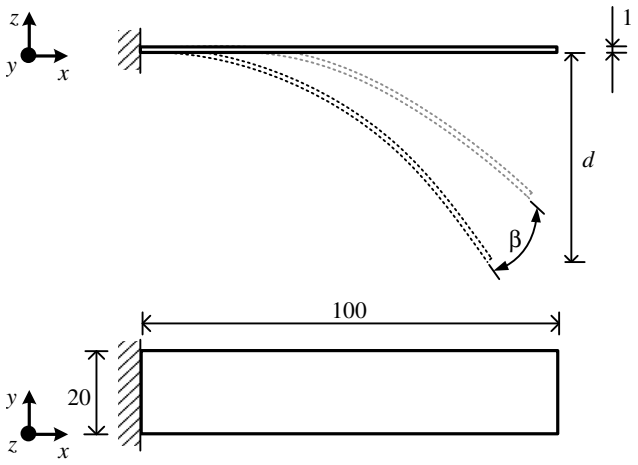

Fig. 13 Simple bending test schematic representation

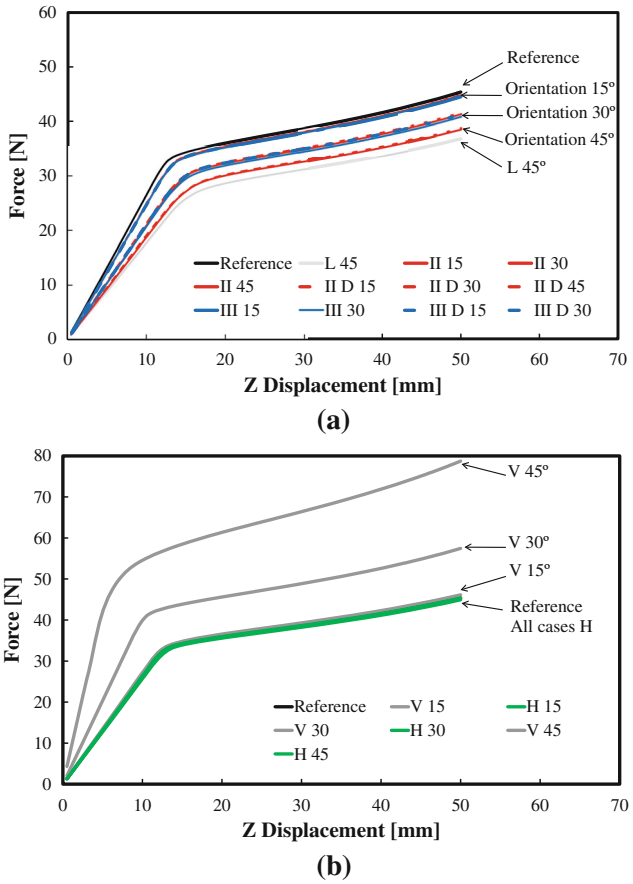

Fig. 14 Bending force versus displacement in z direction for: **a** trimmed meshes: **b** rotated meshes

Finally, for the 45° trimming orientation (Fig. 17), since the elements form a more regular mesh, the strain distribution obtained is closer to the reference mesh. The option of using degenerated elements, to replace the pentahedral-shaped elements, does not seem to improve the accuracy for this mesh orientation (Fig. 17c).

3.4.3 Error analysis

The springback angle, β, was measured for each mesh according to the definition presented in Fig. 13. The normalized percentage error between each mesh and the regular (reference) mesh was calculated as:

$$\text{error}_\beta = 100|\beta - \beta_{\text{ref}}|/|\beta_{\text{ref}}|, \tag{13}$$

being the results presented in Fig. 18a. From this figure, it can be observed that the springback angle shows some variation with the trimmed mesh orientation, being almost independent on the type of boundary elements that result from the different correction methods. It is observed that for trimmed meshes, the springback angle increases with the rotation angle α. The springback angle is almost constant for all H meshes, while for V meshes it strongly decreases with the increase of the rotation angle α. The overall springback variation can be correlated with the previously mentioned θ angle. As shown in Fig. 18b, the difference between the θ angle of trimmed meshes and the reference mesh increases with the rotation angle α of the mesh. In this case the diagonals size of the inner finite element is always the same, but with the increase of the θ angle are less aligned with the bending direction, thus the springback angle increases. The same behavior is valid for the H meshes. However, in this case the variations in θ are smaller leading to a smaller variation of the springback angle. For the V meshes, with the increase of the rotation angle α the longer diagonal increases, becoming also more aligned with the bending direction, i.e., the θ angle decreases. This results in the strong increase of the punch force as well as in the strong decrease of the springback angle.

The interaction between the rotation angle α and the alignment angle θ makes it more difficult to quantify the error associated to the inner finite elements rotation. However, the results indicate that, globally, the use of degenerated elements to correct the pentahedral-shaped elements tends to slightly increase the error in the springback angle. Also, in this case the correction method III leads to a slightly smaller error in the springback angle. This can be related with the fact that this correction method keeps the global orientation of the elements in the specimen width direction.

4 Application examples

DD3TRIM code has been used in pre-processing applications, for mesh generation within blank shape optimization procedures [20, 21]. However, the main application of DD3TRIM code is for multi-step deep-drawing simulations, combined with DD3IMP deep-drawing

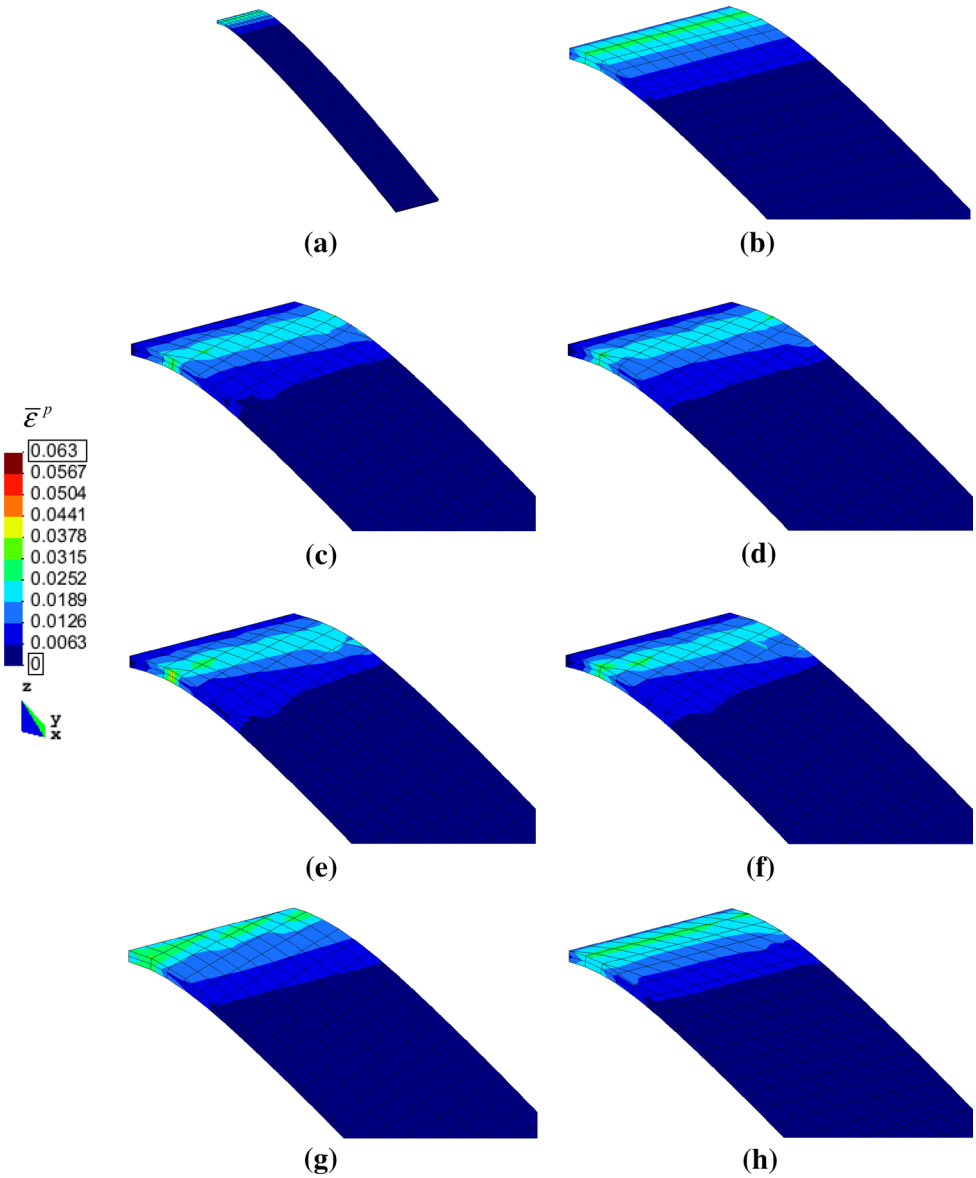

Fig. 15 Equivalent plastic strain distribution in the simple bending test for the reference mesh and meshes with orientation 15°: **a** deformed mesh (*global view*); **b** reference mesh; **c** mesh II; **d** mesh II D; **e** mesh III; **f** mesh III D; **g** mesh V; **h** mesh H

code. In this case, throughout the simulation, along with each mesh modification, a remapping operation is required to transfer the computed data (forces, displacements, stresses, strains, etc.) from the previous (before the trimming/remeshing) to the final mesh (after the trimming/remeshing). For this purpose, the DD3TRIM code includes a remapping algorithm named incremental volumetric remapping [34], based on the weighted average calculus of the intersecting volumes of the two meshes involved in the remapping operation. In the following subsections, the application of DD3TRIM trimming algorithm is shown in two benchmark examples, only to highlight the local character of the changes induced in the finite element mesh by the trimming methodologies proposed.

4.1 Splitting ring test

The first benchmark presented is commonly named "Splitting ring test" and is related with springback prediction. The test methodology consists on cutting a ring specimen from a deep drawn cup and then splitting it along a radial plane. The difference between the ring diameters, before and after splitting, gives a direct measure of the springback that takes place in the ring, due to the residual stresses installed in the cup wall [35].

In this example, the deep drawn cup is trimmed by planes perpendicular to the drawing direction [18, 19]. Figure 19a presents an example of the final configuration of the drawn cup, which is first trimmed by a plane at a depth of 35 mm. The finite element mesh configuration

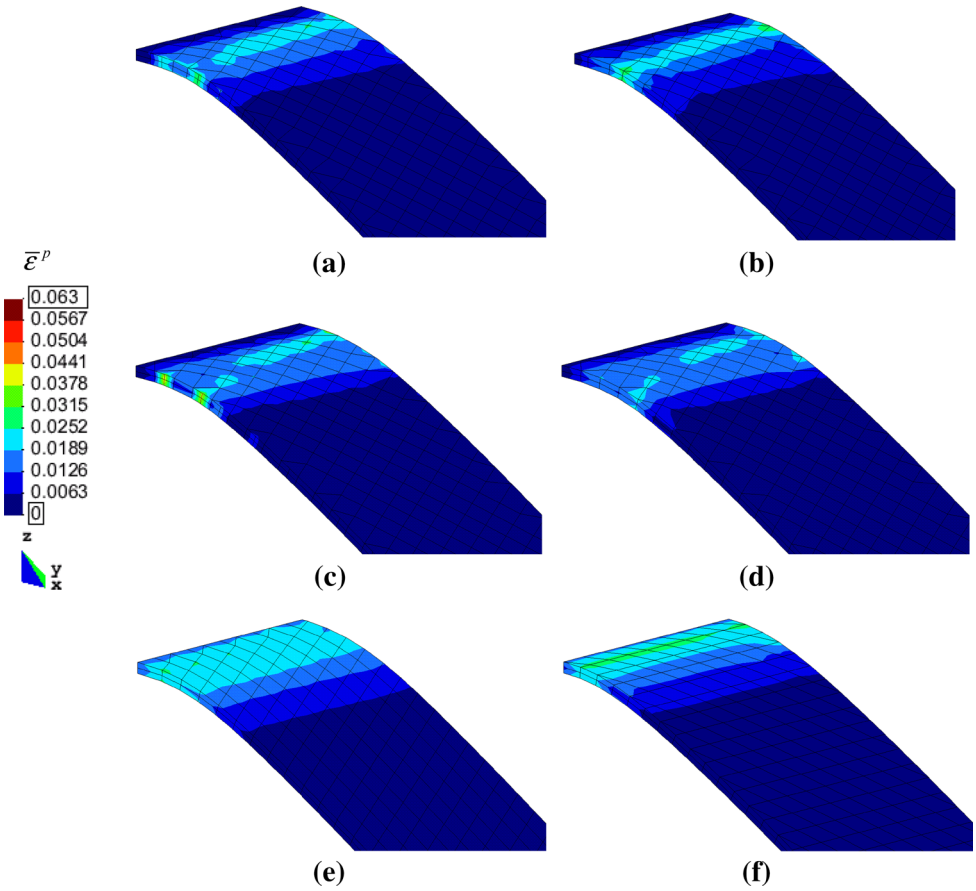

Fig. 16 Equivalent plastic strain distribution in the simple bending test for the meshes with orientation 30°: **a** mesh II; **b** mesh II D; **c** mesh III; **d** mesh III D; **e** mesh V; **f** mesh H

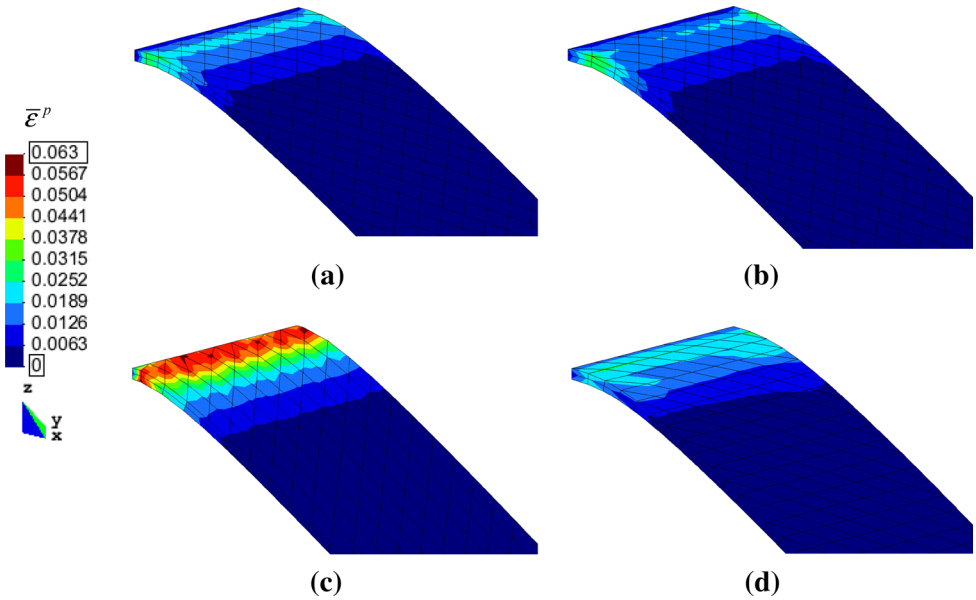

Fig. 17 Equivalent plastic strain distribution in the simple bending test for the meshes with orientation 45°: **a** mesh II; **b** mesh II D; **c** mesh V; **d** mesh H

after this operation is shown in Fig. 19b. Correction type II was selected to minimize the misalignment relative to the inner finite elements. Consequently, for the elements with status "keep", the nodes with "eliminate" status where projected on the plane. The same operation was performed for nodes with status "keep" of elements with status "eliminate". Thus, only four pentahedral-shaped elements appear in the transition between elements with status "keep" and "eliminate". According with the previously presented results, the pentahedral-shaped elements were treated by moving the nodes of the exterior facet of the element to the middle edge position. Afterwards, this mesh

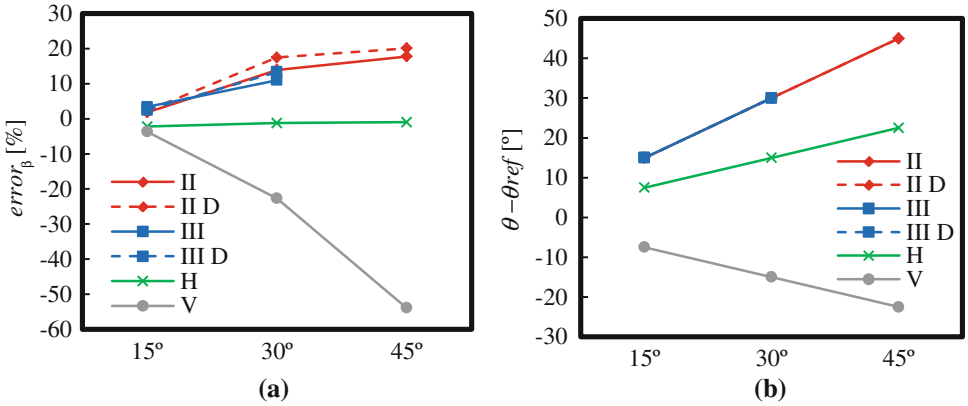

Fig. 18 **a** Springback angle percentage error for each mesh; **b** $\theta - \theta_{ref}$ angle evolution with the rotation angle α

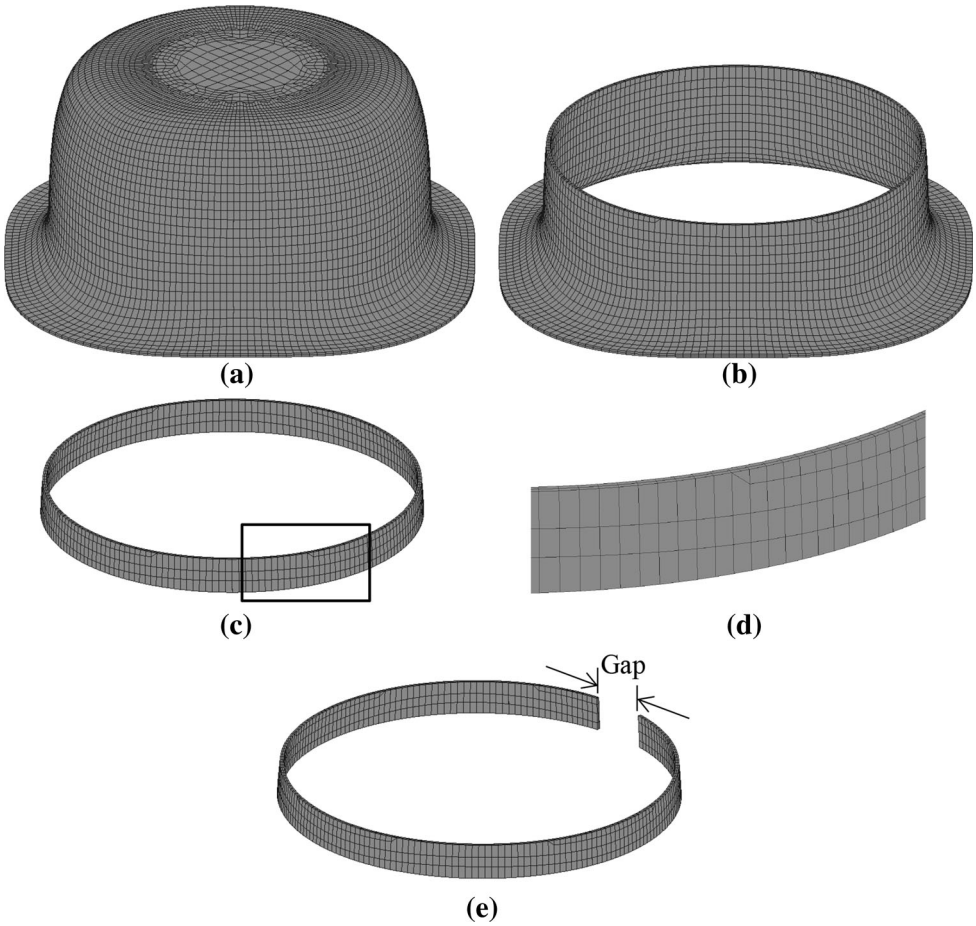

Fig. 19 Schematic description of the splitting ring test simulation stages: **a** drawn cup; **b** trimming the *upper part* of the cup; **c** ring specimen; **d** ring specimen detail; **e** splitting operation: ring after springback

was trimmed by a plane at a depth of 25 mm, to obtain the ring presented in Fig. 19c. In this trimming operation the same correction and treatment methods were selected. However, in this case no treatment is necessary after the correction stage, since no pentahedral-shaped elements appear in the final mesh. The detail of the final ring, presented in Fig. 19d, highlights the treatment method applied. Figure 19e shows the final geometry of the ring, after the splitting operation, which is also defined using DD3TRIM code.

4.2 Equibiaxial–uniaxial strain path change test

This multi-step forming test was developed to better understand the behavior of the constitutive models under pseudo-orthogonal strain path changes during the material deformation process. The material pre-strain in biaxial stretching is achieved by means of the bulge test with a circular die. Figure 20 shows an example of the final configuration of the blank at the end of the numerical simulation of this step. This figure also shows the

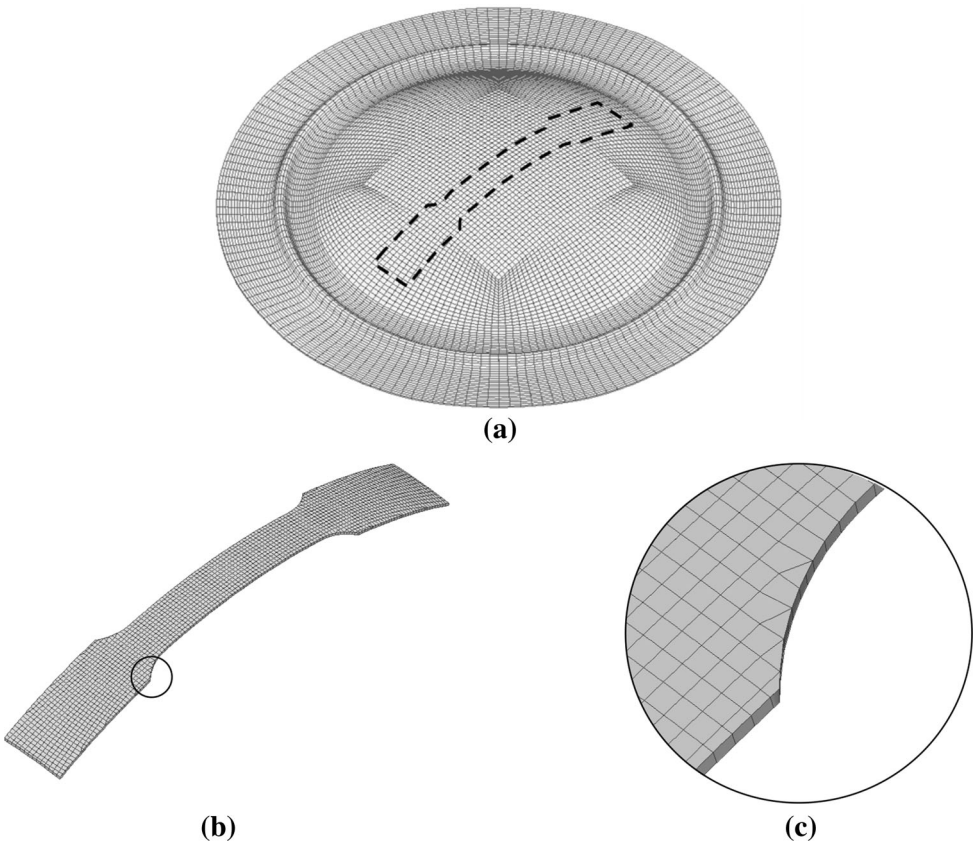

Fig. 20 Equibiaxial-uniaxial strain path simulation test: **a** deformed part after bulge test; **b** trimmed specimen to perform a uniaxial tensile test; tensile test specimen detail

shape and orientation of the normalized tensile specimen that is extracted by trimming the deformed part. Subsequently, this specimen is subjected to a uniaxial tensile test [36].

In this example the cup is trimmed with a complex shape, schematically presented in Fig. 20a. Due to symmetry conditions of the example only a quarter of the tensile test specimen is trimmed from a quarter of the bulge specimen. This involves two trimming operations: (1) by a plane, to define the length of the specimen; (2) by a NURBS surface to define the specimen width. Also in this example, the correction type II was selected for both trimming operations, to minimize the misalignment relative to the inner finite elements. Due to the regular shape of the initial mesh, the trimming operation defined by the plane leads only to hexahedral elements, as shown in Fig. 20b. Along the width, due to a nonlinear shape of the mesh or of the trimming NURBS, some pentahedral-shaped elements appear in the transition between elements with "keep" and "eliminate" status. Their shape was optimized moving the nodes of the exterior facet of the element to the middle edge position, as highlighted in the detail presented in Fig. 20c. The combination of correction and treatment strategies implemented in DD3TRIM algorithm allows performing this complex trimming operation without any user intervention.

5 Conclusions

This paper presents an evaluation of the correction and treatment methodologies implemented in DD3TRIM code, for trimming solid finite element meshes. Only the methodologies that can precisely adjust the mesh to the trimming surface, correction types II and III, were tested. The tests were performed considering an isotropic elastoplastic material with isotropic hardening. The comparison of numerical simulation results between trimmed and rotated meshes, with different orientations to the loading direction, highlights the local effect of the methodologies adopted. In fact, for the tensile test results it is possible to separate the effect of the correction and treatment strategy from the effect of the mesh rotation angle. It was possible to state that the error in the equivalent plastic strain distribution, related with the rotation angle α, is less than 3 %. The increase of this error, for each trimmed mesh, results from the presence of distorted and degenerated elements. The bending test is also sensitive to the mesh orientation towards the bending direction. Thus, it was not possible to separate the influence of mesh rotation angle. Globally, it can be stated that the differences in the numerical simulation results obtained with both correction strategies (II and III) are quite small and depend on the loading direction, i.e., for the tensile test the correction type II leads to smaller errors in the

equivalent plastic strain distribution, while for the bending test correction type III results in lower springback errors. Therefore, the correction strategy should be selected trying to minimize the misalignment with the inner finite elements, but also taking into account the loading direction. Regardless of the treatment strategies applied to treat the pentahedral-shaped elements, there are always some oscillations of the internal state variables along the trimmed borders. These oscillations are narrower when degenerated elements are used but, globally, induce slightly higher errors in the numerical simulation results. Therefore, the relocation of the node in the middle edge methodology seems to be more effective. The application of DD3TRIM to benchmark tests also highlights the local effect of the developed solutions.

Acknowledgments This work was co-financed by the Portuguese Foundation for Science and Technology via project PTDC/EME–TME/103350/2008 and by FEDER via the "Programa Operacional Factores de Competitividade" of QREN with COMPETE reference: FCOMP-01-0124-FEDER-010301.

References

1. Baptista AJ, Alves JL, Rodrigues DM, Menezes LF (2006) Trimming of 3D solid finite element meshes using parametric surfaces: application to sheet metal forming. Finite Elem Anal Des 42:1053–1060. doi:10.1016/j.finel.2006.03.005
2. Choi TH, Choi S, Na KH, Bae HS, Chung WJ (2002) Application of intelligent design support system for multi-step deep drawing process. J Mater Process Technol 130–131:76–88. doi:10.1016/S0924-0136(02)00780-X
3. Kawka M, Kakita T, Makinouchi A (1998) Simulation of multi-step sheet metal forming process by a static explicit FEM code. J Mater Process Technol 80–81:54–59. doi:10.1016/S0924-0136(98)00133-2
4. Yang DY, Ahn DG, Lee CH, Park CH, Kim TJ (2002) Integration of CAD/CAM/CAE/RP for the development of metal forming process. J Mater Process Technol 125–126:26–34. doi:10.1016/S0924-0136(02)00414-4
5. Dalloz A, Besson J, Gourgues-Lorenzon A-F, Sturel T, Pineau A (2009) Effect of shear cutting on ductility of a dual phase steel. Eng Fract Mech 76:1411–1424. doi:10.1016/j.engfracmech.2008.10.009
6. Gram MD, Wagoner RH (2011) Fineblanking of high strength steels: control of material properties for tool life. J Mater Process Technol 211:717–728. doi:10.1016/j.jmatprotec.2010.12.005
7. Husson C, Correia JPM, Daridon L, Ahzi S (2008) Finite elements simulations of thin copper sheets blanking: study of blanking parameters on sheared edge quality. J Mater Process Technol 199:74–83. doi:10.1016/j.jmatprotec.2007.08.034
8. Ghosh S, Li M, Khadke A (2005) 3D modeling of shear-slitting process for aluminum alloys. J Mater Process Technol 167:91–102. doi:10.1016/j.jmatprotec.2004.08.031
9. Li Y-M, Peng Y-H (2003) Fine-blanking process simulation by rigid viscous-plastic FEM coupled with void damage. Finite Elem Anal Des 39:457–472. doi:10.1016/S0168-874X(02)00103-8
10. Saanouni K, Belamri N, Autesserre P (2010) Finite element simulation of 3D sheet metal guillotining using advanced fully coupled elastoplastic-damage constitutive equations. Finite Elem Anal Des 46:535–550. doi:10.1016/j.finel.2010.02.002
11. Menezes LF, Teodosiu C (2000) Three-dimensional numerical simulation of the deep drawing process using solid finite elements. J Mater Process Technol 97:100–106. doi:10.1016/S0924-0136(99)00345-3
12. Oliveira MC, Alves JL, Menezes LF (2003) Improvement of a frictional contact algorithm for strongly curved contact problems. Int J Numer Meth Eng 58:2083–2101. doi:10.1002/nme.845
13. Oliveira MC, Alves JL, Menezes LF (2003) One step springback strategies in sheet metal forming. In: Owen DRJ, Onate E, Suárez B (eds) Proceedings of the 7th International Conference on Computational Plasticity (Complas), Barcelona, p 87
14. Oliveira MC, Alves JL, Chaparro BM, Menezes LF (2007) Study on the influence of work-hardening modeling in springback prediction. Int J Plast 23:516–543. doi:10.1016/j.ijplas.2006.07.003
15. Li KP, Carden WP, Wagoner RH (2002) Simulation of springback. Int J Mech Sci 44:103–122. doi:10.1016/S0020-7403(01)00083-2
16. Coelho LC, Gattass M, Figueiredo LH (2000) Intersecting and trimming parametric meshes on finite element shells. Int J Numer Meth Eng 47:777–800. doi:10.1002/(SICI)1097-0207(20000210)47:4<777:AID-NME797>3.0.CO;2-6
17. Dhondt G (2001) A new automatic hexahedral mesher based on cutting. Int J Numer Meth Eng 50:2109–2126. doi:10.1002/nme.114
18. Laurent H, Grèze R, Oliveira MC, Menezes LF, Manach PY, Alves JL (2010) Numerical study of springback using the split-ring test for an AA5754 aluminum alloy. Finite Elem Anal Des 46:751–759. doi:10.1016/j.finel.2010.04.004
19. Laurent H, Coer J, Grèze R, Manach PY, Andrade-Campos A, Oliveira MC, Menezes LF (2011) Mechanical behaviour and springback study of an aluminium alloy in warm forming conditions. Int Sch Res Netw ISRN Mech Eng :9. doi:10.5402/2011/381615
20. Oliveira MC, Padmanabhan R, Baptista AJ, Alves JL, Menezes LF (2009) Sensitivity study on some parameters in blank design. Mater Des 30:1223–1230. doi:10.1016/j.matdes.2008.06.010
21. Padmanabhan R, Oliveira MC, Baptista AJ, Alves JL, Menezes LF (2009) Blank design for deep drawn parts using parametric NURBS surfaces. J Mater Process Technol 209:2402–2411. doi:10.1016/j.jmatprotec.2008.05.035
22. Livermore Software Technology Corporation (Lstc) (2013) LS-DYNA® keyword user's manual, volume I, Version R7.0. http://www.dynasupport.com/manuals/ls-dyna-manuals/ls-dyna-manual-r-7.0-vol-i
23. McMeeking RM, Rice JR (1975) Finite-element formulations for problems of large elastic-plastic deformation. Int J Solids Struct 11(5):601–616. doi:10.1016/0020-7683(75)90033-5
24. Yamada Y, Yoshimura N (1968) Plastic stress-strain matrix and its application for the solution of elastic-plastic problems by the finite element method. Int J Mech Sci 10(5):343–354. doi:10.1016/0020-7403(68)90001-5
25. International Center For Numerical Methods In Engineering (CIMNE) (2013) GID 11 Reference manual. http://www.gidhome.com/index.php?option=com_content&id=297. Accessed Jan 2013
26. Oliveira MC, Alves JL, Menezes LF (2002) Springback evaluation using 3D finite elements. In: Yang DY, Oh SI, Huh H, Kim YH (eds) Proceedings of the 5th International Conference and workshop on numerical simulation of 3d sheet forming processes (NUMISHEET'2002)—verification of simulation with experiment, vol 1, pp 189–194
27. Padmanabhan R, Oliveira MC, Baptista AJ, Alves JL, Menezes LF (2007) Study on the influence of the refinement of a 3-D finite element mesh in springback evaluation of plane-strain channel sections. In: César de Sá JMA, Santos AD (eds) Proceedings of the 9th International Conference in numerical methods in

industrial forming processes (NUMIFORM'07), American Institute of Physics Conference, vol 908, pp 847 852. doi:10.1063/1.2740916
28. Teodosiu C (1989) The plastic spin: microstructural origin and computational significance. In: Owen DRJ, Hinton E, Onate E (eds) Proceedings of the 2nd Int. Conf. on Computational Plasticity, Barcelona, p 163
29. Alves JL, Oliveira MC, Menezes LF (2004) An advanced constitutive model in sheet metal forming simulation: the Teodosiu microstructural model and the Cazacu Barlat yield criterion. In: Glosh S, Castro JC, Lee JK (eds) Proceedings of the Numiform'04 on materials processing and design: modelling, simulation and applications. Amer Inst Physics, Melville, p 1645
30. Bouvier S, Alves JL, Oliveira MC, Menezes LF (2005) Modelling of anisotropic work-hardening behaviour of metallic materials subjected to strain path changes. Comput Mater Sci 32(3–4): 301–315
31. Hughes TJR (1980) Generalization of selective integration procedures to anisotropic and nonlinear. Int J Numer Meth Eng 15:1413–1418
32. Menezes LF, Teodosiu C, Makinouchi A (1991) 3-D solid elastoplastic elements for simulating sheet metal forming processes by the finite element method. In: Berichte VDI (ed) Proceedings FE-simulation of 3-D sheet metal forming processes in automotive industry. VDI VERLAG, Dusseldorf, pp 381–403
33. Alves JL, Menezes LF (2001) Application of tri-linear and tri-quadratic 3-D solid finite elements in sheet metal forming simulations. In: Mori K-I (ed) Proceedings of the Numiform'01 on Simulation of materials processing: theory, methods and applications. Balkema, Rotterdam, pp 639–644
34. Baptista AJ, Alves JL, Oliveira MC, Rodrigues DM, Menezes LF (2005) Application of the incremental volumetric remapping method in the simulation of multi-step deep drawing processes. In: Smith LM, Zhang L, Wang C-T, Shi MF, Yoon J-W, Stoughton TB, Cao J, Pourboghrat F (eds) Proceedings of the 6th International Conference and workshop on numerical simulation of 3d sheet metal forming processes (NUMISHEET). Melville, New York, p 173
35. Demeri MY, Lou M, Saran MJ (2000) A benchmark test for springback simulation in sheet metal forming. Soc Automot Eng 01:2657. doi:10.4271/2000-01-2657
36. Li S, Hoferlin E, Van Bael A, Van Houtte P, Teodosiu C (2003) Finite element modelling of plastic anisotropy induced by texture and strain-path change. Int J Plast 19:647–674. doi:10.1016/S0749-6419(01)00079-1